ACS APPLIED MATERIALS & INTERFACES

www.acsami.org
Research Article

Polyethylene Glycol-Protected Zinc Microwall Arrays for Stable Zinc Anodes

Zehao Song, Chengwu Yang, Napat Kiatwisarnkij, Anqi Lu, Naraphorn Tunghathaithip, Kittima Lolupiman, Thiti Bovornratanaraks, Xinyu Zhang,* Guanjie He,* and Jiaqian Qin*

Cite This: https://doi.org/10.1021/acsami.4c15130
Read Online

ACCESS | Metrics & More | Article Recommendations | Supporting Information

ABSTRACT: Aqueous zinc-ion batteries promise good commercial application prospects due to their environmental benignity and easy assembly under atmospheric conditions, positioning them as a viable alternative to lithium-ion batteries. However, some inherent issues, such as chaotic zinc dendrite growth and inevitable side reactions, challenge the commercialization progress. In this work, we imprint highly ordered zinc microwall arrays to regulate the electric field toward uniform Zn deposition. Afterward, coating a polyethylene glycol protection layer on the zinc microwalls aims to passivate the surface defects that rise unintentionally by mechanical imprinting. Polyethylene glycol can also boost oriented Zn deposition along the (002) plane and inhibit hydrogen gas production, further enhancing the stability of such three-dimensional (3D) hybrid anodes. Compared to the messy electric field near the polyethylene glycol-protected Zn foil, the uniform electric field provided by these 3D hybrid anodes can regulate the Zn deposition behaviors, enabling a longer lifespan and thus certifying the necessity of adding 3D microstructures. Additionally, 3D microstructures can offer a larger surface area than that of the planar Zn foil, providing more reaction sites and higher specific capacity. In this case, the 3D hybrid electrode exhibits a good initial capacity of approximately 120 mA h/g at a current density of 5 A/g and a nice retention of more than 80% after 800 cycles. The proposed scheme paves the way for a long-term stable 3D zinc anode solution with promising application prospects.

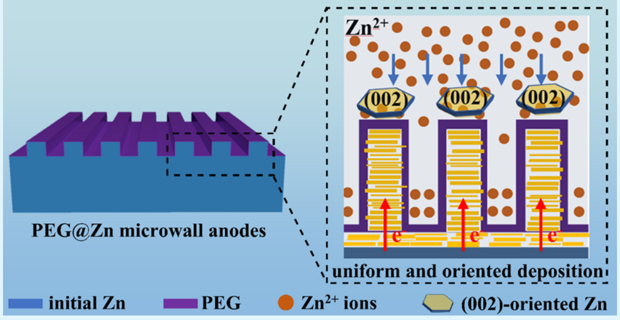

KEYWORDS: *aqueous zinc-ion batteries, 3D microwall array, mechanical imprint technology, polyethylene glycol, dendrite suppression, enhanced lifespan*

1. INTRODUCTION

Today's grid-scale energy storage systems support the promising possibility of utilizing renewable energy by storing and redistributing reasonable power supply and demand.[1] For example, as a typically renewable energy source, wind commonly occurs for a short period, requiring the energy storage system with high energy density to quickly store the generated electricity.[2] Owing to high energy density and good rechargeability, remarkable progress has been witnessed in the studies of lithium-ion batteries in recent decades.[3−5] Nevertheless, the safety and environmental pollution issues arising from the utilization of organic electrolytes in lithium-ion batteries push scientists to find safer and more environmentally friendly alternatives.[6] Among the various candidates, aqueous zinc-ion batteries successfully grasp mass attention due to their high theoretical specific capacity (820 mA h/g), relatively low reoxidation potential (−0.76 V vs SHE), low price, and excellent safety properties.[7−14] However, the commercial applications of zinc-ion batteries still need many developments to solve two inherent challenges of the zinc (Zn) anode (i.e., the chaotic Zn dendrite growth and the parasitic hydrogen evolution reaction). Due to the strong anisotropy of the Zn crystal lattice in the hexagonal close-packed pattern, the Zn dendrite growth fundamentally exhibits the uncontrolled feature.[15] The mass transport during the Zn stripping/plating processes is another essential factor causing uncontrolled Zn dendrite growth. The continuously uncontrolled Zn dendrite growth would adjust the localized field, making it more disordered, referred to as the "tip effect", consequently resulting in battery failure.[16−18] In addition, the hydrogen evolution reaction initially accompanies the Zn electrodeposition according to the thermodynamic theory.[19] It negatively impacts the reversibility of zinc-ion batteries by interrupting the pH distribution and generating inactive byproducts (e.g., zinc oxides or hydroxides).[20]

Received: September 5, 2024
Revised: November 6, 2024
Accepted: November 6, 2024

ACS Publications

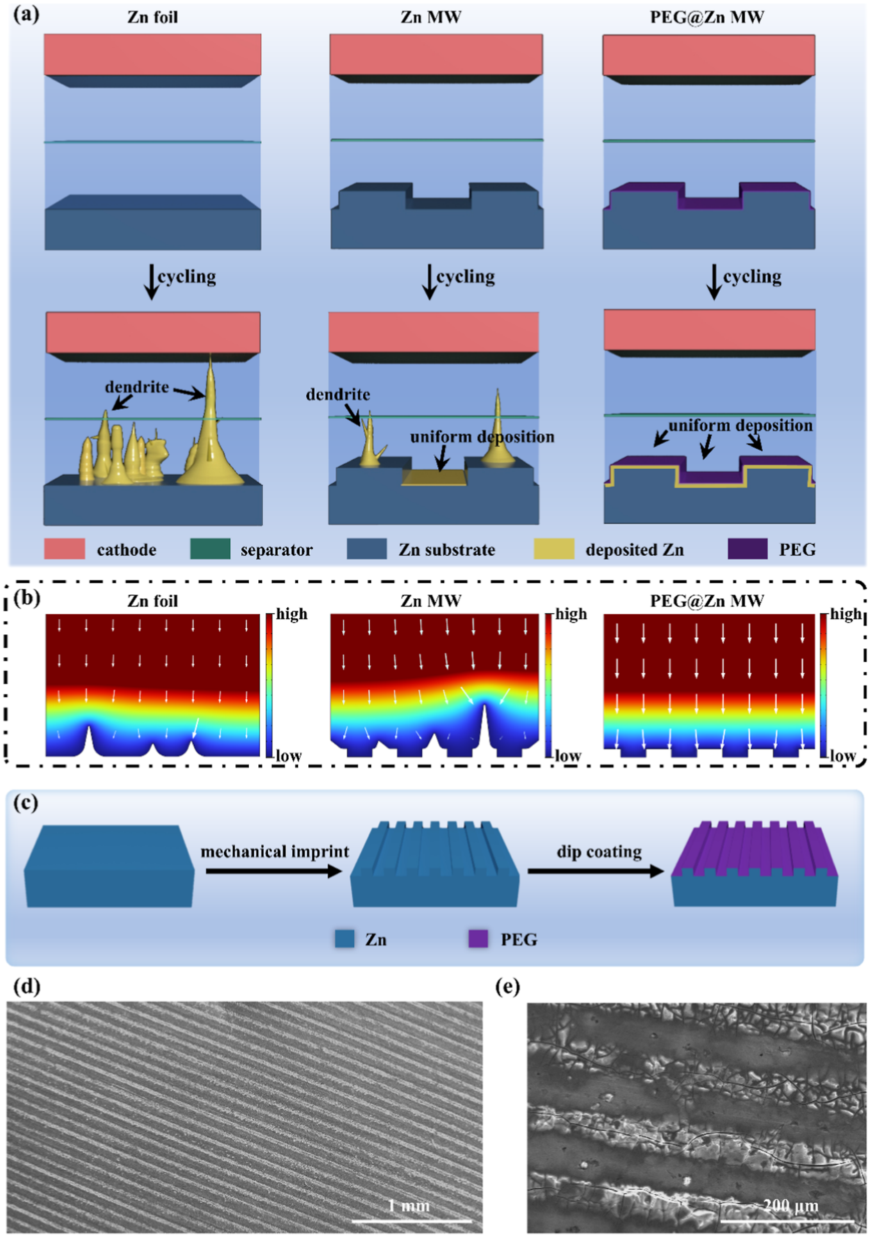

Figure 1. (a) Comparison of different anodes for Zn plating. The left, middle, and right panels demonstrate the different Zn deposition on the Zn foil, Zn MW, and PEG@Zn MW, respectively. The upper panels illustrate the initial cases of anodes, and the bottom ones show the corresponding states after cycling. (b) COMSOL simulation of electric field for the Zn foil (left), Zn MW (middle), and PEG@Zn MW (right) in a possible case. The color gradient represents the magnitude of electrolyte potential, wherein the colors dark pink and blue demonstrate the maximum and minimum values, respectively. The arrows illustrate the direction and magnitude of the current density at different locations. A longer arrow suggests a higher current density at a certain point inside the electrolyte. (c) Schematic of the fabrication process applied for the PEG@Zn MW anode. (d) Global morphology of the PEG@Zn MW anode. (e) Corresponding local view of the PEG@Zn MW anode.

Many approaches have been developed to inhibit the Zn dendrite growth, such as coating an artificial interface layer, constructing three-dimensional (3D) nano/micro-structures or rebuilding (002)-oriented Zn texture.[20−23] The 3D Zn microstructure can induce the uniform electric field in the vicinity of the anode, further leading to the controlled migration of Zn ions, consequently resulting in the uniform Zn deposition and the effective suppression of the dendrite growth. Nevertheless, this modification strategy can only prompt the uniform Zn deposition in the bottom trench, whereas some Zn dendrites can grow on the top of the 3D microstructures.[24] Additionally, some unintentional mechanical failure during the imprinting process would inevitably cause surface defects on the Zn MWs, which can conduct a messy local electric field, prompting the dendrite growth during the electrochemical cycling. Therefore, it requires an artificial layer to protect the surface of 3D Zn microstructures. In other electrochemical batteries (e.g., lithium-ion or sodium-ion batteries), the solid electrolyte interphase layer is automatically generated to protect the anode from undesired reactions.[25] Because of the highly corrosive activity of the aqueous electrolytes (e.g., $ZnSO_4$, $ZnCl_2$), the inherent solid electrolyte interphase layer is difficult to produce.[21] In this view, some materials, such as poly(vinylidene fluoride) (PVDF), poly(ethylene oxide), zinc sulfide, zinc fluoride, and tin, are employed as the artificial interface layer to protect the

https://doi.org/10.1021/acsami.4c15130
ACS Appl. Mater. Interfaces XXXX, XXX, XXX−XXX

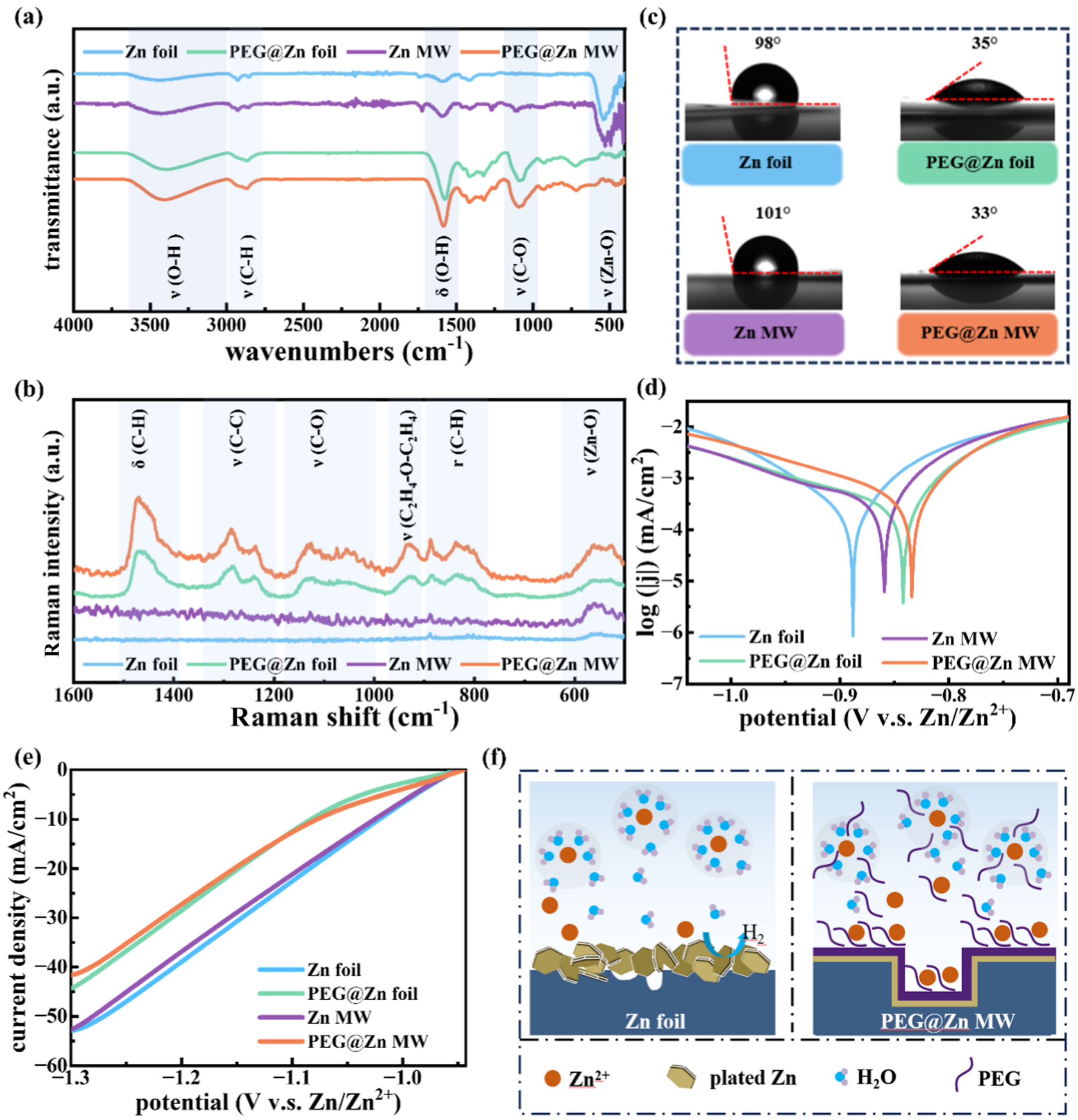

Figure 2. (a) FTIR spectroscopy of four types of anodes, measured in an ambient atmosphere at room temperature. (b) Corresponding Raman spectroscopy in the fingerprint region (i.e., 1500−500 cm^{-1}). The symbols ν, δ, and r in panels a and b represent stretching, bending, and rocking vibration modes, respectively. (c) Contact angles on the surface of different anodes where they meet the deionized water droplet. (d) Potentiodynamic polarization curves measured from four different anodes in 2 M $ZnSO_4$ aqueous solution at room temperature. (e) Linear sweep voltammetry curves of different anodes in the 2 M $ZnSO_4$ aqueous solution. (f) Mechanism of PEG in the zinc-ion batteries.

Zn surface. A good material candidate applied for the artificial interface layer should feature several basic characterizations, including electrical insulation, a good hydrophile, and a solid ability to suppress hydrogen evolution reactions. If it is more outstanding, it should exhibit the potential to modify the nucleation/growth process of the Zn deposition, enabling (002)-oriented Zn plating behaviors. Because the (002) plane features lower hydrogen evolution activity and horizontal surface, compared to the (100) and (101) planes.[26]

Herein, we demonstrate the application of a 3D poly(ethylene glycol) (PEG) protected Zn microwall array in zinc-ion batteries, enabling the simultaneous suppression of Zn dendrite growth and the inhibition of hydrogen evolution. Among the various materials for Zn surface protection, the following advantages significantly contribute to our decision in favor of PEG: (1) the ability to promote the oriented Zn deposition along the (002) plane,[27] fundamentally inhibiting the dendrite growth; (2) strong interaction with the water molecules,[28] suppressing the hydrogen evaluation reactions; (3) a low electronic conductivity but a good ionic conductivity,[29] enabling the homogeneous Zn deposition below the artificial protection layer;[30] (4) outstanding mechanical properties including good flexibility and elasticity,[31,32] adapting to the volumetric deformation of Zn microstructures during the cycling; and (5) good adhesion,[27,33] avoiding the detachment from the Zn microstructure surface during the plating/stripping process, thereby achieving long-term protection and good lifetime. Consequently, such 3D hybrid anodes demonstrate a longer lifetime in the symmetric cells compared to the Zn foils. Its full batteries paired with the vanadium oxide (V_2O_5) cathodes also show enhanced specific capacity and stability.

2. RESULTS AND DISCUSSION

Figure 1a demonstrates the mechanism of three different zinc-based anodes. The left panels of Figure 1a depict the typical plating behaviors on Zn-foil-based anodes in aqueous zinc-ion batteries. The bare Zn foil suffers severe dendrite issues in the mild aqueous electrolytes (i.e., 2 M $ZnSO_4$ aqueous solution), resulting in the inhomogeneous deposition of Zn during cycling, thereby leading to the uncontrolled growth of Zn dendrites. The planar Zn foil can be constructed into 3D micro/nanostructures to alleviate the dendrite problem, as 3D structures can regular the electric field distribution, making Zn ions evenly depositing. The middle panels of Figure 1a illustrate Zn microwalls (Zn MWs) used in this work, enabling uniform Zn deposition in the trenches between adjacent microwalls. However, chaotic dendrite growth may still occur on the top of Zn MWs, due to the lack of significant conductivity difference between the top surface of Zn MWs and their trenches.[24] Therefore, during the Zn plating process, Zn deposition would not perform any preferential selection between the top surface and the trenches. Compared to the planar foils, the 3D microstructures normally can concentrate the current, enabling a higher current density and thereby increasing the possibility of dendrite growth.[24] These undesired dendrites could make the uniform electric field disorder again, strengthening the short-circuit risk. To avoid this trouble, we construct PEG@Zn MWs, protecting the exposed surfaces of Zn MWs in the aqueous electrolyte. With the coating of PEG, Zn can be evenly deposited at the interface between PEG and Zn MW.[30]

Figure 1b illustrates the possible electric field distribution in the vicinity of three anodes after a few cycles of charging/discharging. Graduated colors illustrate the change of the electrolyte potential near the electrodes. The direction and length of the arrows represent the flow orientation and the magnitude of the current density at points in the electrolyte, respectively. With respect to the Zn foil, dendrites in different sizes induce various local electric field distributions and current densities in their vicinity (please see the left panel of Figure 1b). In particular, the highest value significantly alters its local electric field, enabling a tip-shaped distribution. Besides, a larger current flows toward the top of another dendrite compared to the other points in the electrolyte. Such a chaotic electric field can further worsen the Zn deposition, resulting in a short-circuit issue. The messy electric field distribution and current density also appear near the dendrites grown on the top surface of Zn MWs (please see the middle panel of Figure 1b). With the PEG protection, Zn MWs would not grow dendrites immediately after the first few cycles, enabling a uniform electric field and long-term stability. The right panel of Figure 1b demonstrates a uniform electric field distribution near the PEG@Zn MW anode. The lengths of the arrows are almost the same, whereas the directions are random. It suggests a uniform Zn deposition on both the microwalls and trenches in this 3D hybrid anode.

Figure 1c demonstrates the fabrication process of the PEG@Zn MW anode based on the combination of mechanical imprint and dip-coating methods. Using a homemade master mold (please see the detailed information regarding the master mold in Figure S1), the bare Zn foil was mechanically imprinted to produce a 3D Zn MW array on one side, with an average depth of approximately 15 μm, referred to as the Zn MW anode. After imprinting, each microwall is continuous without any visible breaks, suggesting the high-quality pattern transfer technique based on the mechanical imprint (Figure S2). Nevertheless, some surface defects appear on the surface of Zn MWs. Afterward, a PEG protection layer covers the surface of the Zn MW anode via the dip-coating method, assembling the PEG@Zn MW anode. Before investigating the Zn MW anode, the PEG layer has already been optimized for the Zn foil anode (Figures S3 and S4). Compared to the other two concentrations of aqueous PEG solution, the PEG protection layer prepared by the 600 mg/mL solution exhibits the best stability, enabling the longest lifetime of more than 200 h at the applied current density of 5 mA/cm^2 and the areal capacity of 1 mA h/cm^2.

Figure 1d demonstrates the homogeneous morphology of the PEG@Zn MW anode with the well-aligned 3D microwall array in a large area of 4 × 2 mm. The enlarged scanning electron microscopy (SEM) image of the PEG@Zn MW anode in Figure 1e depicts the surface of the Zn MW well protected by PEG. The cross-section image of PEG@Zn MWs depicts a Ω-shaped PEG coating layer formed atop the Zn MWs with an average thickness of approximately 12 μm (Figure S5a). The corresponding energy-dispersive X-ray elemental mapping analysis also illustrates clear profiles of the microwalls (Figure S5b−d).

Figure 2a illustrates Fourier-transform infrared (FTIR) spectroscopy of Zn foil, Zn MW, PEG@Zn foil, and PEG@Zn MW in the range from 4000 to 400 cm^{-1}. With respect to the Zn foil, the peak located at around 541 cm^{-1} originates from the Zn−O stretching vibration mode of the native oxide on the Zn surface.[34] The O−H stretching and bending vibration modes of the attached water molecules correspond to the peaks at 3445 and 1593 cm^{-1}, respectively.[28] As bare Zn foils were subsequently cleaned by acetone and ethanol, the residual acetone and(or) ethanol molecules are likely to absorb on the Zn surface, thereby resulting in two peaks at 2930 and 2855 cm^{-1} (corresponding to the C−H and CH_2−CH_2 stretching modes, respectively).[35] After coating the PEG protection layer the peak of the CH_2−CH_2 stretching vibration mode highly increases, even merging with the peak of the C−H stretching vibration mode, consequently causing a broad one in the FTIR spectroscopy of PEG@Zn foil and PEG@Zn MW.[36] FTIR spectroscopy only illustrates the significant peaks in the functional group region; while the peaks in the fingerprint region seem chaotic, with some important ones absent. The Raman spectroscopy in Figure 2b demonstrates the typical fingerprint peaks in the range from 1600 to 500 cm^{-1}. One shoulder at 1472 cm^{-1} is assigned to the bending vibration of the C−H bonds.[37] Besides, the peaks between 1300 and 1000 cm^{-1} are related to the twisted side group of the PEG molecule. The peaks at 1282 and 1131 cm^{-1} originate from the vibrational PEG conformation gauche modes of the C−C and C−O bonds, respectively. Additionally, the bands at 1235 and 1127 cm^{-1} are caused by the vibrational PEG conformation trans modes of the C−C and C−O bonds, respectively. The stretching vibration of the CH_2−O−CH_2 bonds in the main chain generates one peak at 937 cm^{-1}. The band composed of two peaks at 860 and 843 cm^{-1} is contributed to by the antisymmetric rocking vibrational modes of the C−H bonds. By combining the results of FTIR and Raman spectroscopy, we can claim that the PEG protection layer has been successfully deposited on the surface of Zn foil and Zn MW anodes.

Figure 2c depicts contact angles between the deionized water droplet and the surface of the anodes. The metal zinc normally exhibits natural hydrophilicity, enabling liquid contact angles less than 90°.[38] However, the native zinc oxide on the surface of the zinc foil could slightly weaken the

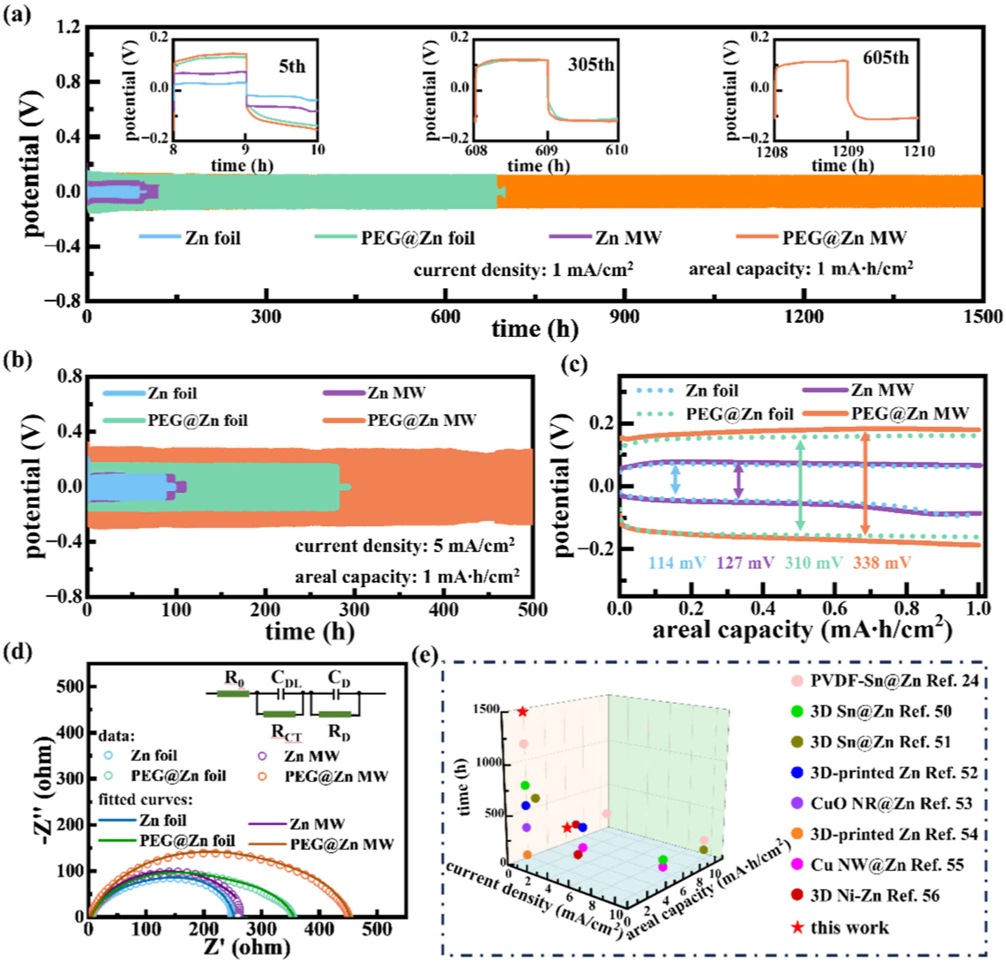

Figure 3. (a) Stability of the symmetric batteries assembled by different anodes. The current density and the areal capacity are set to be 1 mA/cm^2 and 1 mA h/cm^2, respectively. The insets demonstrate detailed potential curves at different cycles. (b) Corresponding stability under a current density of 5 mA/cm^2 and a areal capacity of 1 mA h/cm^2. (c) Potential as the function of the areal capacity, which is derived from panel b. Four types of electrodes demonstrate different overpotential hysteresis at an areal capacity of 0.4 mA h/cm^2. Please note that we separate the arrow annotations to make them more beautiful. Their actual position should be at an areal capacity of 0.4 mA h/cm^2. (d) Electrochemical impedance spectrum of different electrodes at room temperature. The inset illustrates the equivalent electric circuit applied for the charge transfer resistance R_{CT} fitting. R_0 represents electrolyte bulk resistance, which normally dominates in the high-frequency region. C_{DL} and R_{CT} denote the double-layer capacitance and the charge-transfer resistance at middle frequency, respectively. R_D and C_D are resistance and capacitance caused by the slow ion diffusion at low frequencies, respectively. (e) Comparison between the PEG@Zn MW electrode and other 3D microstructure electrodes in terms of lifespan.

wettability, resulting in a higher contact angle.[39] In this case, the measured contact angle of 98° indicates the formation of native zinc oxide on the bare Zn foil's surface, which agrees with the measurement results from other reports.[40,41] As an amphiphilic polymer, PEG can significantly improve wettability,[42] enabling a smaller contact angle of 35° after being deposited on the Zn foil. According to the prediction of the Wenzel model,[43] the surface roughness can act as an amplifier to enlarge the inherent hydrophilicity (and hydrophobicity) properties of solid materials, that is, the increased surface roughness makes a hydrophilic material more hydrophilic, and vice versa for hydrophobic materials. Compared with the Zn foil, Zn MWs with the 3D artificial microstructures feature higher surface roughness, exhibiting more hydrophobicity with a larger contact angle of 101°. Due to the conversion from hydrophobicity to hydrophilicity via coating the PEG protection layer, PEG@Zn MW with a higher surface roughness becomes more hydrophilic than PEG@Zn foil.

Figure 2d shows the free corrosion potential E_{corr} of four types of anodes defined as the turning point between the anodic and cathodic zones of the potentiodynamic polarization curve. The corroding system for the potentiodynamic polarization measurements comprises Pt and Ag/AgCl as the counter and reference electrodes, respectively. Potentiodynamic polarization measurements were run in an aqueous electrolyte of 2 M $ZnSO_4$ at room temperature. The polarization curve of the Zn foil electrode consists of two distinct parts, representing the anodic and cathodic reaction process of the Zn foil, respectively. The turning point corresponds to the free corrosion potential of E_{corr} = −0.888 V for the Zn foil, which is in agreement with other reports.[27] The PEG layer atop the Zn foil electrode weakens the surface correction reactions, resulting in a significant shift of free corrosion potential E_{corr} in the potentiodynamic polarization curves (i.e., shift from −0.888 to −0.842 V). Compared to the Zn foil electrode, the free corrosion potential E_{corr} of the Zn MW electrode increases to E_{corr} = −0.859 V, likely due to the surface roughness change.[44] The PEG@Zn MW electrode exhibits the highest corrosion resistivity with a free corrosion potential of $E_{corr} = -0.834$ V.

Figure 2e demonstrates linear sweep voltammetry (LSV) curves of different electrodes in a 2 M $ZnSO_4$ aqueous solution. Compared to the Zn foil, the LSV curve of the PEG@Zn foil depicts a smaller slope, thereby suggesting a better HER suppression capability. Furthermore, the microwall morphology causes a negligible change in the slope by comparing the LSV curves of Zn foil and Zn MW (or PEG@Zn foil v.s. PEG@Zn MW). The morphology modification seems to have no significant impact on the HER in our case. Therefore, the PEG protection layer mainly determines the improved electrochemical stability. Xie et al. claimed that the strengthened H−O covalent bond in the water molecules enables higher electrochemical stability because of the hydrogen-bonding interaction between the O atom of PEG and the H atom of H_2O.[28] The oxygen atom in PEG performs a higher negative charge than that in water due to the electron-donating effect of alkyl groups. This effect in PEG decreases the oxygen atom electron-attracting capability, weakening the hydrogen bonding between water and PEG molecules, in contrast to the stronger hydrogen bonding observed between water molecules.[45] Hou et al. stated that coating the PEG layer atop the Zn anode can effectively avoid direct contact between Zn and water molecules.[27] In this case, we suppose that both effects should simultaneously contribute. Due to the high solubility of PEG in water at room temperature, a part of PEG should be dissolved in the electrolyte, acting as the electrolyte additive. The FTIR spectrum of the 2 M $ZnSO_4$ electrolyte in Figure S6 demonstrates a blue shift of the H−O stretching peak after being immersed by a PEG@Zn foil electrode for 24 h, due to the interaction between PEG and H_2O inside the electrolyte. Besides, the FTIR spectroscopy of PEG@Zn MW still illustrates the typical peaks of PEG after running for 500 cycles in a 2 M $ZnSO_4$ electrolyte (please see Figure S7). Therefore, some PEG molecules can remain on the Zn surface while others are dissolved in the electrolyte, as shown in Figure 2f.

In order to explore the cyclic stability and electrochemical profiles of modified anodes, we assemble the symmetric cells with Zn foil, PEG@Zn foil, Zn MW, and PEG@Zn MW (henceforth denoted as Zn foil||Zn foil, PEG@Zn foil||PEG@Zn foil, Zn MW||Zn MW, and PEG@Zn MW||PEG@Zn MW, respectively) and then evaluate their long-term stability under various current densities (Figure 3a,b). Concerning the long-term cycling measurements at a current density of 1 mA/cm^2 and a areal capacity of 1 mA h/cm^2 (Figure 3a), Zn MW||Zn MW exhibits a slightly prolonged cycle life of 95 h, compared to Zn foil||Zn foil. Compared to the bare Zn foil, the limited lifespan improvement of Zn MWs may be caused by some possible reasons mentioned before, including the lack of preferential selection for Zn deposition on the top surface or trenches, a higher current density near the top surface of Zn MWs and unintentional surface defects caused by the mechanical imprinting fabrication method. For PEG@Zn foil||PEG@Zn foil, the PEG protection layer enables a significant enhancement with a cyclic lifetime of more than 600 h. Due to the 3D hybrid structure enabling the functionalities of regulating electric field distribution and shielding the Zn surface simultaneously, PEG@Zn MW||PEG@Zn MW performs a good cyclic lifetime of more than 1500 h. In contrast to the chaotic electric field near the PEG@Zn foil electrodes, the uniform field provided by the 3D microwall array in the PEG@Zn MW can further enhance the stability, even though the PEG layer protects both electrodes. The inset of Figure 3a demonstrates the individual potential profiles of different anodes at various cycles. At the fifth cycle, all four types of anodes exhibit favorable potential responses to charging−discharging pulses. However, due to the short-circuit issues, only PEG@Zn foil and PEG@Zn MW anodes maintain responses at the 305th cycle. Furthermore, only the PEG@Zn MW anode continues to display a response, highlighting its good long-term stability.

At a higher current density of 5 mA/cm^2 and a fixed areal capacity of 1 mA h/cm^2 (Figure 3b), we can conclude the same results regarding the stability of anodes (i.e., PEG@Zn MW > PEG@Zn foil > Zn MW > Zn foil). Nevertheless, the difference in the overpotential between these four types of anodes becomes more apparent at the higher current density. Figure 3c illustrates a comparison of the overpotentials of anodes derived from the second cycles of their galvanostatic cycling measurements at a current density of 5 mA/cm^2. Compared to a small overpotential hysteresis of 114 mV for Zn foil||Zn foil, PEG@Zn foil||PEG@Zn foil demonstrates a large hysteresis of 310 mV due to the impact of the PEG protection layer. The increase of the overpotential hysteresis should be attributed to the passivation of the electrochemically active sites on the Zn surface, where the PEG molecules preferentially adsorb.[45] The high surface overpotential is helpful in forming the high nucleation overpotential and the small critical size of nuclei, thus resulting in the uniform plating of Zn (please see Figure S8).[46] Compared to the Zn foil||Zn foil, the slightly enhanced overpotential hysteresis of Zn MW||Zn MW may originate from the alteration of the surface roughness by building the 3D artificial Zn MW array. On the other hand, the higher current density can inherently increase the overpotential hysteresis.[26,47] The overpotential difference between PEG@Zn foil and PEG@Zn MW electrodes is enlarged at a current density of 5 mA/cm^2, compared to that at a current density of 1 mA/cm^2. The rate-performance testing also supports this argument (see Figure S9). Additionally, the PEG@Zn MW anode exhibits a higher exchange current density than the PEG@Zn foil, corresponding to a slower deposition kinetic. Figure S10 indicates similar results to those in Figure 3a,b, but with a shorter lifespan at a large current density of 10 mA/cm^2. Furthermore, the PEG@Zn MW anode can also work well with a lifetime of more than 100 h at a high current density of 20 mA/cm^2 and a large areal capacity of 10 mA h/cm^2 (please see Figure S11). Nevertheless, the PEG@Zn foil anode only remains a short lifetime of 15 h at such a high current density, as the large local electric field would prompt the Zn dendrite growth resulting in the short-circuit issue at a high current density (please see Figure S12). Therefore, compared to the simple PEG-protection strategy, the good lifetime of the PEG@Zn MW anode at a high current density highlights the importance of utilizing the hybrid strategy to protect the anode surface and regulate the electric field simultaneously. Figure S13 suggests good Coulombic efficiencies of approximately 100% for both the Zn foil and PEG@Zn MW electrodes.

The increased surface overpotential is highly related to the enhancement of charger-transfer resistance R_{CT}.[48] Figure 3d illustrates Nyquist plot evolution for four types of electrodes in the initial states. To extract the charge-transfer resistance from Nyquist plots, we employ an equivalent electric circuit model

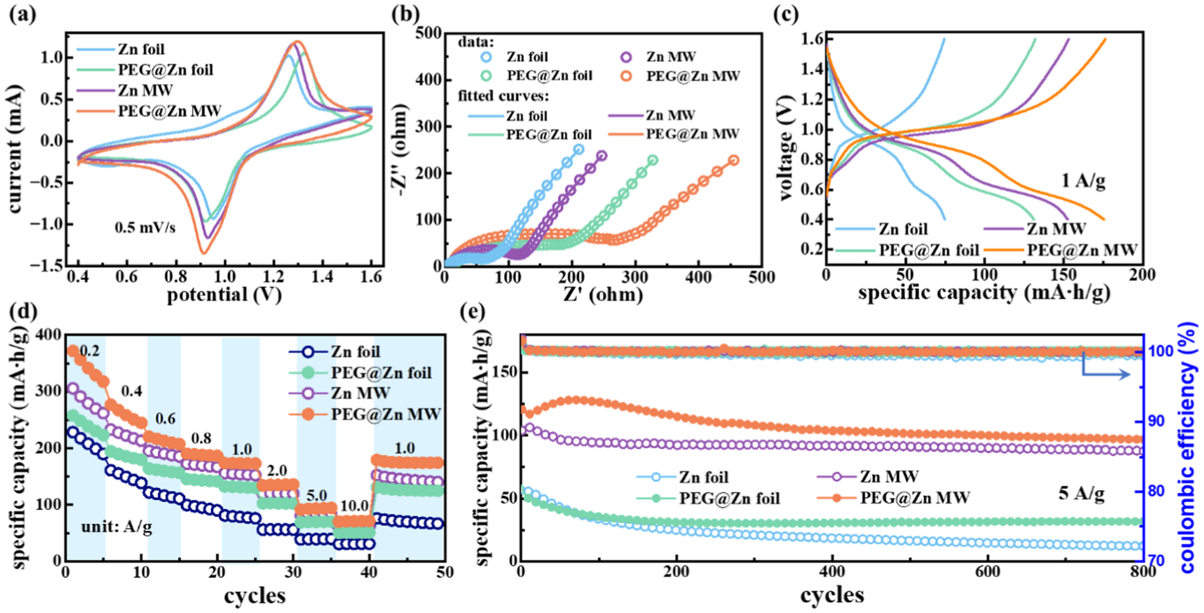

Figure 4. (a) CV curves of different full batteries, when vanadium oxide V_2O_5 works as the cathode. The sweeping rate is 0.5 mV/s. (b) EIS of these full batteries in the initial state. (c) Galvanostatic charge−discharge curves under the current density of 1 A/g. (d) Rate performances of different full batteries. (e) Comparing long-term cycling performances of these full batteries at a current density of 5 A/g.

composed of the electrolyte bulk resistance R_0, the double-layer capacitance C_{DL}, the charge-transfer resistance R_{CT}, the ion diffusion resistance R_D, and capacitance C_D, depicted in the inset of Figure 3d. The charger-transfer resistance R_{CT} is fitted as 94.8, 246.6, 275.4, and 345.4 Ω for the Zn foil, Zn MW, PEG@Zn foil, and PEG@Zn MW electrode, respectively. Both modification methods (i.e., adding the PEG protection layer to shield the Zn surface and constructing 3D microstructures to regular the electric field) can strengthen charger-transfer resistance, resulting in higher surface overpotential, which is in agreement with the results derived from Figure 3c. A large surface overpotential can strengthen the nucleation overpotential and reduce the critical size of nuclei, resulting in a smaller dendrite size and more uniform current distribution at a given current density, consequently leading to more uniform Zn deposition and better long-term stability.[49] Figure 3e summarizes the lifetime of the 3D Zn electrodes. Compared to the other 3D Zn electrodes, our PEG@Zn microwall electrode exhibits a good lifespan.[24,50−56]

To demonstrate the feasibility of our PEG@Zn MW anodes in a practical scenario, we assembled full batteries using a vanadium oxide V_2O_5 cathode (please see the X-ray diffraction (XRD) analysis and morphology of V_2O_5 in Figure S14), a 2 M $ZnSO_4$ electrolyte, and a 200 μm thick glass microfiber filter. All four types of anodes are applied to assemble different full cells, including Zn foil‖V_2O_5, PEG@Zn foil‖V_2O_5, Zn MW‖V_2O_5, and PEG@Zn MW‖V_2O_5. Figure 4a illustrates the cyclic voltammetry (CV) curves of various full batteries at a sweeping rate of 0.5 mV/s. With respect to Zn foil‖V_2O_5, the CV curve demonstrates two reduction peaks at the voltage of approximately 0.52 and 0.95 V, corresponding to the insertion of Zn^{2+} and H^+ ions into the V_2O_5 cathode. Additionally, the oxidation peak located at 1.26 V should originate from the extraction process of Zn ions from V_2O_5. Compared to Zn foil‖V_2O_5, the reduction peak of PEG@Zn foil‖V_2O_5 and PEG@Zn MW‖V_2O_5 related to H^+-ion insertion exhibits position shifts. It should be contributed to the additive of the PEG protection layer atop the anode, which is in agreement with the results derived from the LSV curves in Figure 2e. Figure 4b depicts the electrochemical impedance spectrum (EIS)s of different full cells, which were tested in the initial state without any cycling. The charge-transfer resistances of Zn foil‖V_2O_5, PEG@Zn foil‖V_2O_5, Zn MW‖V_2O_5, and PEG@Zn MW‖V_2O_5 are fitted to be 64.8, 214.0, 109.4, and 264.7, respectively. In agreement with the results observed from the symmetric batteries in Figure 3d, the charge-transfer resistance subsequently increases in the following order: Zn foil‖V_2O_5, Zn MW‖V_2O_5, PEG@Zn foil‖V_2O_5, and PEG@Zn MW‖V_2O_5.

Figure 4c illustrates the galvanostatic charge−discharge (GCD) performance of these full cells under a current density of 1 A/g. With respect to the discharge part, all four curves show a distinct sequence: an initial linear region with a rapid voltage drop from 1.6 V to approximately 1.0 V, followed by a sublinear region with a slow descent to 0.8 V, then the second linear and sublinear region lasting from 0.8 to 0.5 V, and finally a fast drop to 0.4 V. The turning points between linear and sublinear regions appear around 1.0 and 0.6 V for the first and second parts, respectively, which is in agreement with the reduction peaks in the CV curves in Figure 4a. The first sublinear region located between 1.0 and 0.8 V suggests that such zinc-ion batteries can supply electric power in the range of 1.0−0.8 V for devices in the practical scenario.

Figure 4d presents the rate performances under various current densities. Zn foil‖V_2O_5 demonstrates a fast reduction from 228.1 to 30.3 mA h/g, while the current density gradually increases from 0.2 to 10 A/g. Due to the protective effect of the PEG layer, PEG@Zn foil‖V_2O_5 presents an improved rate performance; that is, its capacity drops from 257.6 to 50.5 mA h/g with increasing the current density. As the microstructures can remarkably increase the surface area, providing more reaction sites, Zn MW‖V_2O_5 exhibits larger capacity than Zn foil‖V_2O_5 and PEG@Zn foil‖V_2O_5 under overall current densities with a good rate performance as well (i.e., a decrease from 305.4 to 58.8 mA h/g). The combination of the protection of PEG and the sufficient surface area of the microstructures enables the best rate performance among these

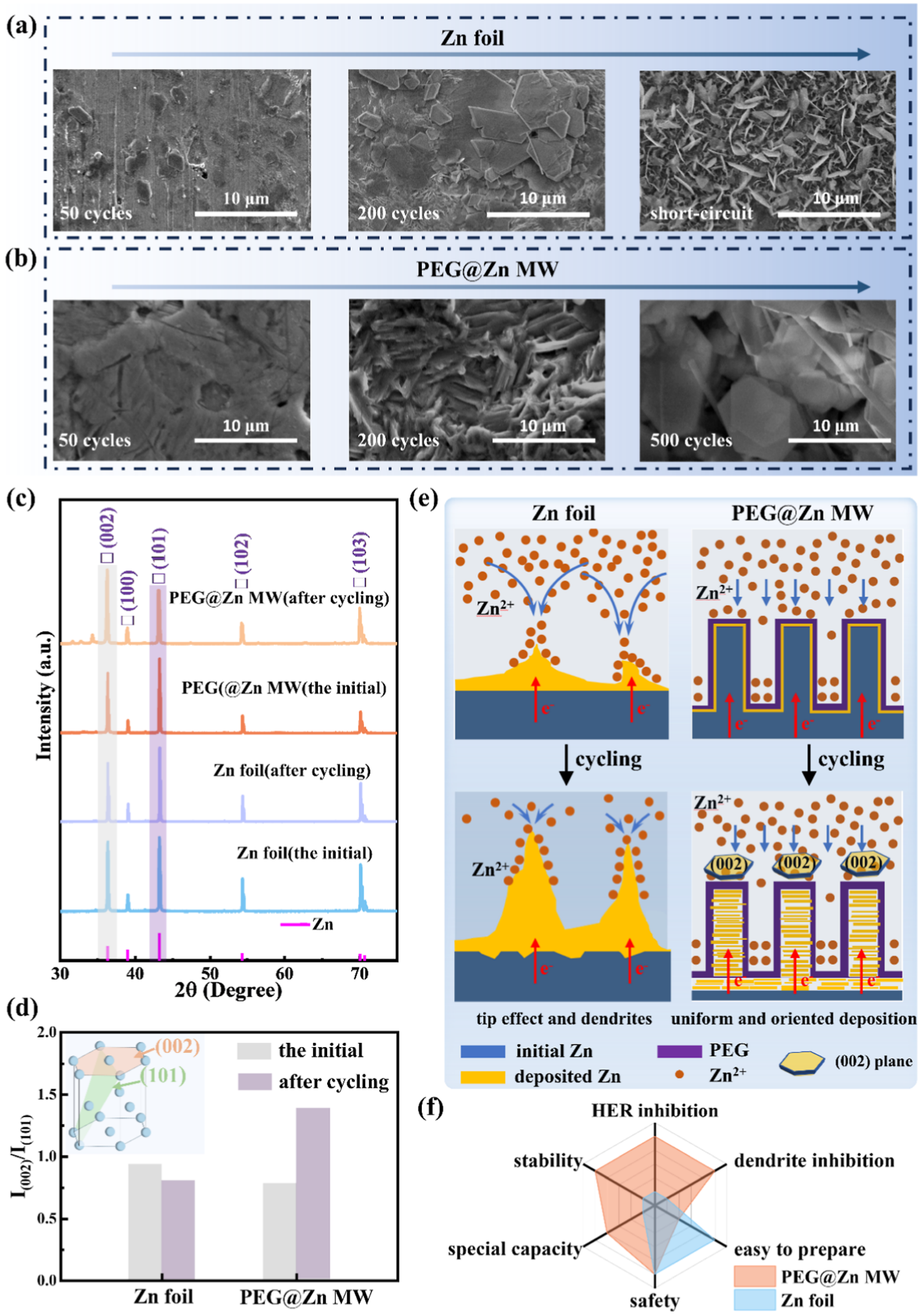

Figure 5. (a) SEM images of Zn foils after galvanostatic testing in symmetric cells. The left, middle, and right panels demonstrate the morphology of the Zn foil after 50 cycles, 200 cycles, and being short-circuit, respectively. The applied current density and the areal capacity are 5 mA/cm^2 and 1 mA h/cm^2, respectively. (b) The corresponding SEM images of PEG@Zn MW anodes. (c) Comparison of XRD patterns between Zn foil and PEG@Zn MW anodes before and after cycling. (d) Calculated intensity ratio of $I_{(002)}/I_{(101)}$ between (002) and (101) peaks of Zn foil and PEG@Zn MW anodes. The inset illustrates the profile of the (002) and (101) plane. (e) Possible theory explaining the plating behaviors of Zn foil and PEG@Zn MW anodes. (f) Comparing the different performances of Zn foil and PEG@Zn MW electrodes via radar chart plotting.

four types of full batteries, which is observed from PEG@Zn MW||V_2O_5 with a drop from 371.7 to 70.1 mA h/g. Furthermore, the current density was set back to 1 A/g after the gradual increase to 10 A/g, in order to characterize the reversibility in such rechargeable batteries. All four types of full batteries present excellent reversibility with a ratio of approximately 100% at a current density of 1 A/g. Figure 4e displays the cycling stability of these full batteries at a high current density of 5 A/g. Compared to Zn foil||V_2O_5 (with capacity retention of 21.4%), PEG@Zn foil||V_2O_5 performs better stability with a capacity retention of 64.2% after 800 cycles, although their initial capacity is almost the same. Both Zn MW||V_2O_5 and PEG@Zn MW||V_2O_5 exhibit excellent retentions of more than 80%. Table S1 suggests a comparable performance of full batteries paired with our PEG@Zn MW to other advanced batteries.[24,50−56]

Figure 5a,b depicts the change of the anode surface morphology with continuous cycling. The global morphology of the Zn foil anode almost remains flat, with some defects in the partial regions after the first 50 cycles. Nevertheless, some of the flat regions then become chaotic as well after 200 cycles. Finally, the whole area is in the crowd of inclined Zn nanosheets. Unlike the Zn foil anode, PEG@Zn MW shows a modified surface morphology after the initial plating and eventually demonstrates a stack of planar hexagonal Zn nanosheets. Compared to the planar Zn nanosheets, the shape edge of the inclined Zn nanosheets would alter the local electric field, strengthening the "tip" effect, resulting in the growth of the dendrites and the impairment of the separator. The formation of the inclined Zn nanosheets should be contributed to the preferable growth of the (101) plane of the Zn foil anode under a large current, as the (101) plane features high surface energy in the 2 M $ZnSO_4$ electrolyte.[47] By comparison of the XRD patterns of Zn foil before and after cycling, the ratio of peak intensities drops from 0.94 to 0.78, thus reflecting the enhancement of the (101) plane after cycling (Figure 5c,d). In contrast, PEG can boost the favorable plating in the (002) plane.[27] In Figure 5c,d, compared to the initial state, the (002) peak of the PEG@Zn MW is higher than the (101) peak, enabling a ratio of $I_{(001)}/I_{(101)}$ of 1.39 after cycling. Therefore, the PEG protective layer can adjust the plating behavior of the Zn anode, prompting (002)-oriented deposition. Figure S15 demonstrates the in situ observations of Zn deposition on the different anodes. Both Zn dendrites and hydrogen gas (H_2) bubbles appear on the surface of the Zn foil. However, the PEG@Zn MW electrode can maintain the shape of the microwall without any Zn dendrites and H_2 bubbles during the plating process. After plating, Zn foil features a messy surface morphology, whereas the PEG@Zn MW electrode displays distinct uniform stripes. (See Figure S16). Therefore, the microstructures of the PEG@Zn MW electrode would not immediately disappear after a few cycles, continuously regulating the electric field and resulting in the uniform Zn deposition.

According to the combination of SEM and XRD results, we propose one possible principle to explain the highly extended lifespan of the PEG@Zn MW electrode. In the left panels of Figure 5e, the dendrites grown on the Zn foil surface trigger a tip effect, leading to a chaotic electric field. After further cycling, the tip effect can enhance the size of the dendrites, making the electric field distribution even worse, eventually causing short-circuit issues. Unlike the Zn foil, the PEG@Zn MW electrode can induce a uniform electric field near its surface, enabling the homogeneous deposition of Zn ions (see the right panels in Figure 5e). In the subsequent cycling process, the (002)-oriented deposition can also avoid short-circuit problems, due to the modification effect of PEG on the crystal growth.

Figure 5f summarizes the different properties of the Zn foil and the PEG@Zn MW electrode. Compared to the Zn foil, the PEG@Zn MW electrode demonstrates a large improvement in dendrite inhibition, HER inhibition, stability, and special capacity. However, the electrode requires a slightly more complex fabrication process than the Zn foil. Although utilizing the PEG layer in this case, the aqueous electrolyte can prevent the zinc-ion batteries from spontaneously combusting at high temperatures. Therefore, the safety can remain good, even though adding a PEG protection layer on the 3D Zn microstructures.

3. CONCLUSIONS

In conclusion, we have demonstrated the feasibility of constructing 3D hybrid microstructures toward long-term stable zinc anodes by combining the regulation of the electric field distribution with surface shielding. The PEG protection layer can prompt (002)-oriented Zn deposition and suppress the hydrogen evolution reaction, enabling the PEG@Zn foil to perform a longer lifespan than the Zn foil. Compared with the Zn foil, the Zn MW electrode features a larger surface area and a regular electric field distribution, thereby achieving significant improvement in specific capacity and stability. Compared to PEG@Zn foil and Zn MW based on the individual strategy, the 3D hybrid microstructures exhibit even stronger stability and better capacity performances. Therefore, even with the surface protection layer, a uniform electric field provided by 3D microstructures is still indispensable for the ultralong-term stable zinc anode. This work primarily illustrates the feasibility of the hybrid strategy via small-area mechanical imprinting and simple dip-coating technology. Nevertheless, the industry can employ roll-to-plate or roll-to-roll imprinting methods to manufacture large-area Zn anodes.

4. EXPERIMENTAL SECTION

4.1. Materials. Ammonium metavanadate (NH_4VO_3) (purity of ≥99%) and 1-methyl-2-pyrrolidinone (purity of 99%) were produced by Sigma-Aldrich. PVDF with a purity of ≥99.5% and conductive acetylene black with a resistivity of ≤1.8 Ω/m were produced by MTI Corporation. The Zn foil with a thickness of 100 μm was purchased from Präzisionsfolien GmbH. The conductive carbon paper with a thickness of 200 μm and a resistivity of 580 MΩ/m was purchased from Toray Industries, Inc.

4.2. Preparation of Zn Foil Electrode. A Zn foil was tailored into the smaller circular slides with a diameter of 14 mm by a precision disc cutting machine (MSK-T10, Shenzhen KejingStar Technology Co. Ltd.). Subsequently, the circular Zn slides were washed in deionized water, acetone, and ethanol by the ultrasonic cleaning technique and finally dried in an ambient atmosphere at 348 K.

4.3. Preparation of Zn MW Electrode. A homemade imprint mold was constructed via the laser etching technique, enabling linear gratings with a fixed period of 100 μm and grating line width of 50 μm. In the mechanical imprint process, a Zn foil was positioned flat on top of the imprint mold. Then, a 10 MPa downward pressure supplied by a tablet press machine (TOB-H24T-300A, Xiamen TOB New Energy Technology Co. Ltd.) was loaded on the Zn foil in an ambient atmosphere at room temperature to transfer microstructures from the mold to the Zn foil. Afterward, the Zn foil was carefully separated from the imprint mold and cut into smaller circle slides. Finally, the circular Zn slides with the imprinted microstructures were washed and dried via a process similar to that for the Zn foil electrode.

4.4. Preparation of PEG@Zn Foil Electrode. With respect to the PEG@Zn foil electrode, the steps for tailoring, cleaning, and drying were the same as those for the Zn foil electrode. Nevertheless, a dip-coating step was conducted to cover the circular Zn slide with the PEG protective layer before the cleaning and drying steps. In detail, 6 g of PEG was dissolved in 10 mL of deionized water, forming an aqueous PEG solution. Next, the circular Zn slide was immersed into the aqueous PEG solution and then raised vertically from the solution at a slow velocity.

4.5. Preparation of PEG@Zn MW Electrode. In order to fabricate the PEG@Zn MW electrode, we employed the same tailoring, imprinting, cleaning, and drying methods from the fabrication process of the Zn MW electrode and the dip-coating technique from the preparation of the PEG@Zn foil electrode.

4.6. Material Characterization. XRD analysis was conducted by a Bruker D8 advance X-ray diffractometer. The scanning electron microscope (SEM. Hitachi S4800) was employed to characterize the

https://doi.org/10.1021/acsami.4c15130

morphologies of different electrodes. Bruker. Water contact angles were measured on a DM-CEI instrument in the ambient atmosphere. Confocal images were delivered by a 3D measuring laser microscope (Olympus LEXT OLS5000). A Fourier transform infrared spectrometer was conducted via a FTIR microscope (ThermoFisher Scientific iN10) in the range of 400−4000 cm^{-1}. The Raman microscopy (HORIBA model iHR-550) coupled with a 532 nm laser source was applied to analyze the Raman spectrum.

4.7. Electrochemical Measurements. In order to prepare the V_2O_5 powder, ammonium metavanadate (NH_4VO_3) was annealed in ambient air at 673 K for 2 h. Afterward, the powder was carefully milled to avoid the aggregation of V_2O_5 nano/microparticles. Finally, a composite slurry composed of V_2O_5, conductive acetylene black, and PVDF (in a weight ratio of 7:2:1) was blade-coated atop the conductive carbon paper with an assistance of 120 μm thick film applicator, enabling a mass loading of approximately 1.0 mg for V_2O_5 on the cathode electrode. To meet the requirements of CR2032 coin cells, we precisely cut the anodes and cathodes in circular pieces with a diameter of 14 mm. The cathode, separator, and anode were well aligned from center to center to avoid the wrong active area calculation caused by the position shift. To ensure the thorough wetting of the V_2O_5 cathode, the glass fiber separator, and the anode, 220 μL of 2 M $ZnSO_4$ aqueous electrolyte was added. The three types of batteries were assembled in this work, including symmetric cells, asymmetric cells paired with a copper electrode, and full cells with a V_2O_5 cathode. The NEWARE battery testing system carried out all the GCD measurements at the fixed temperature of 298 K.

The CV of full batteries and the chronoamperometry of symmetric batteries were measured by an electrochemical potentiostat (CHI 660e, Chenhua). The LSV and potentiodynamic polarization curves were measured via a three-electrode system, including a Zn working electrode, a platinum counter electrode, and a silver/silver chloride (Hg/HgCl) reference electrode. The 2 M $ZnSO_4$ aqueous electrolyte was employed again while measuring the LSV and potentiodynamic polarization curves.

■ ASSOCIATED CONTENT

Supporting Information

The Supporting Information is available free of charge at https://pubs.acs.org/doi/10.1021/acsami.4c15130.

Morphology of the master mold and different electrodes and various battery measurements of these electrodes (PDF)

■ AUTHOR INFORMATION

Corresponding Authors

Xinyu Zhang − *State Key Laboratory of Metastable Materials Science and Technology, Yanshan University, Qinhuangdao 066004, P. R. China*; Email: xyzhang@ysu.edu.cn

Guanjie He − *Christopher Ingold Laboratory, Department of Chemistry, University College London, London WC1H 0AJ, U.K.*; orcid.org/0000-0002-7365-9645; Email: g.he@ucl.ac.uk

Jiaqian Qin − *Center of Excellence on Advanced Materials for Energy Storage, Department of Materials Science, Faculty of Science and Center of Excellence on Petrochemical and Materials Technology, Chulalongkorn University, Bangkok 10330, Thailand*; orcid.org/0000-0002-9166-3533; Email: jiaqian.q@chula.ac.th

Authors

Zehao Song − *Metallurgy and Materials Science Research Institute, Chulalongkorn University, Bangkok 10330, Thailand*; orcid.org/0000-0003-3276-7516

Chengwu Yang − *Metallurgy and Materials Science Research Institute, Chulalongkorn University, Bangkok 10330, Thailand; State Key Laboratory of Metastable Materials Science and Technology, Yanshan University, Qinhuangdao 066004, P. R. China*

Napat Kiatwisarnkij − *Metallurgy and Materials Science Research Institute, Chulalongkorn University, Bangkok 10330, Thailand*

Anqi Lu − *Metallurgy and Materials Science Research Institute, Chulalongkorn University, Bangkok 10330, Thailand*

Naraphorn Tunghathaithip − *Extreme Conditions Physics Research Laboratory and Center of Excellence in Physics of Energy Materials(CE:PEM), Department of Physics, Faculty of Science, Chulalongkorn University, Bangkok 10330, Thailand*

Kittima Lolupiman − *Metallurgy and Materials Science Research Institute, Chulalongkorn University, Bangkok 10330, Thailand*

Thiti Bovornratanaraks − *Extreme Conditions Physics Research Laboratory and Center of Excellence in Physics of Energy Materials(CE:PEM), Department of Physics, Faculty of Science, Chulalongkorn University, Bangkok 10330, Thailand*

Complete contact information is available at: https://pubs.acs.org/10.1021/acsami.4c15130

Author Contributions

Z.S., N.K., and C.Y. conducted the fabrication and measurements. Z.S. and A.L. drew the 3D images. Z.S., N.T., and T.B. measured the Raman Spectra. Z.S. and K.L. carried out the XRD tests. J.Q., X.Z., and G.H. conceived the project and contributed essentially to the experimental design. All authors analyzed the results and agreed on the manuscript.

Notes

The authors declare no competing financial interest.

■ ACKNOWLEDGMENTS

This work was supported by the National Research Council of Thailand (NRCT) and Chulalongkorn University (N42A660383), Thailand Science Research and Innovation Fund Chulalongkorn University, and National Natural Science Foundation of China (grant no. 52125405 and U22A20108). Z.S. would like to acknowledge the support from C2F postdoc fellowship, Chulalongkorn University. J.Q. thanks the Hub of Talents: Sustainable Materials for Circular Economy, National Research Council of Thailand (NRCT).

■ REFERENCES

(1) Kabeyi, M. J. B.; Olanrewaju, O. A. Types of Grid Scale Energy Storage Batteries. *Green Energy Technol.* **2024**, *F2329*, 181−203.

(2) Díaz-González, F.; Sumper, A.; Gomis-Bellmunt, O.; Villafáfila-Robles, R. A Review of Energy Storage Technologies for Wind Power Applications. *Renew. Sustain. Energy Rev.* **2012**, *16* (4), 2154−2171.

(3) Li, M.; Lu, J.; Chen, Z.; Amine, K. 30 Years of Lithium-Ion Batteries. *Adv. Mater.* **2018**, *30* (33), 1800561.

(4) Wu, F.; Maier, J.; Yu, Y. Guidelines and Trends for Next-Generation Rechargeable Lithium and Lithium-Ion Batteries. *Chem. Soc. Rev.* **2020**, *49* (5), 1569−1614.

(5) Masias, A.; Marcicki, J.; Paxton, W. A. Opportunities and Challenges of Lithium Ion Batteries in Automotive Applications. *ACS Energy Lett.* **2021**, *6* (2), 621−630.

(6) Costa, C. M.; Barbosa, J. C.; Gonçalves, R.; Castro, H.; Campo, F. J. D.; Lanceros-Méndez, S. Recycling and Environmental Issues of Lithium-Ion Batteries: Advances, Challenges and Opportunities. *Energy Storage Mater.* **2021**, *37* (February), 433−465.

(7) Zhang, N.; Chen, X.; Yu, M.; Niu, Z.; Cheng, F.; Chen, J. Materials Chemistry for Rechargeable Zinc-Ion Batteries. *Chem. Soc. Rev.* **2020**, *49* (13), 4203−4219.

(8) Du, W.; Ang, E. H.; Yang, Y.; Zhang, Y.; Ye, M.; Li, C. C. Challenges in the Material and Structural Design of Zinc Anode towards High-Performance Aqueous Zinc-Ion Batteries. *Energy Environ. Sci.* **2020**, *13* (10), 3330−3360.

(9) Guo, N.; Huo, W.; Dong, X.; Sun, Z.; Lu, Y.; Wu, X.; Dai, L.; Wang, L.; Lin, H.; Liu, H.; Liang, H.; He, Z.; Zhang, Q. A Review on 3D Zinc Anodes for Zinc Ion Batteries. *Small Methods* **2022**, *6* (9), 1−24.

(10) Lv, W.; Meng, J.; Li, X.; Xu, C.; Yang, W.; Duan, S.; Li, Y.; Ju, X.; Yuan, R.; Tian, Y.; Wang, M.; Lyu, X.; Pan, P.; Ma, X.; Cong, Y.; Wu, Y. Boosting Zinc Storage in Potassium-Birnessite via Organic-Inorganic Electrolyte Strategy with Slight N-Methyl-2-Pyrrolidone Additive. *Energy Storage Mater.* **2023**, *54*, 784−793.

(11) Lv, W.; Meng, J.; Li, Y.; Yang, W.; Tian, Y.; Lyu, X.; Duan, C.; Ma, X.; Wu, Y. Inexpensive and Eco-Friendly Nanostructured Birnessite-Type δ-MnO2: A Design Strategy from Oxygen Defect Engineering and K+ Pre-Intercalation. *Nano Energy* **2022**, *98*, 107274.

(12) Lv, W.; Shen, Z.; Li, X.; Meng, J.; Yang, W.; Ding, F.; Ju, X.; Ye, F.; Li, Y.; Lyu, X.; Wang, M.; Tian, Y.; Xu, C. Discovering Cathodic Biocompatibility for Aqueous Zn−MnO2 Battery: An Integrating Biomass Carbon Strategy. *Nano-micro Lett.* **2024**, *16* (1), 109.

(13) Lolupima, K.; Cao, J.; Zhang, D.; Yang, C.; Zhang, X.; Qin, J. A Review on the Development of Metals-Doped Vanadium Oxides for Zinc-Ion Battery. *J. Met., Mater. Miner.* **2024**, *34* (3), 2084.

(14) Mawintorn, T.; Lolupiman, K.; Kiatwisarnkij, N.; Woottapanit, P.; Karnan, M.; Saneewong Na Ayuttay, S.; Zhang, X.; Wangyao, P.; Qin, J. Fabrication and Characterization of Zinc Anode on Nickel Conductive Cloth for High-Performance Zinc Ion Battery Applications. *J. Met., Mater. Miner.* **2024**, *34* (3), 2083.

(15) Li, G.; Sun, L.; Zhang, S.; Zhang, C.; Jin, H.; Davey, K.; Liang, G.; Liu, S.; Mao, J.; Guo, Z. Developing Cathode Materials for Aqueous Zinc Ion Batteries: Challenges and Practical Prospects. *Adv. Funct. Mater.* **2024**, *34* (5), 2301291.

(16) Li, Z.; Beyene, T. T.; Zhu, K.; Cao, D. Realizing Fast Plating/Stripping of High-Performance Zn Metal Anode with a Low Zn Loading. *J. Met., Mater. Miner.* **2024**, *34* (2), 2009.

(17) Lolupiman, K.; Wangyao, P.; Qin, J. Electrodeposition of Zn/TiO2 Composite Coatings for Anode Materials of Zinc Ion Battery. *J. Met., Mater. Miner.* **2019**, *29* (4), 120−126.

(18) Abdulla, J.; Cao, J.; Wangyao, P.; Qin, J. Review on the Suppression of Zn Dendrite for High Performance of Zn Ion Battery. *J. Met., Mater. Miner.* **2020**, *30* (3), 1−8.

(19) Nie, C.; Wang, G.; Wang, D.; Wang, M.; Gao, X.; Bai, Z.; Wang, N.; Yang, J.; Xing, Z.; Dou, S. Recent Progress on Zn Anodes for Advanced Aqueous Zinc-Ion Batteries. *Adv. Energy Mater.* **2023**, *13* (28), 230606.

(20) Zhu, C.; Li, P.; Xu, G.; Cheng, H.; Gao, G. Recent Progress and Challenges of Zn Anode Modification Materials in Aqueous Zn-Ion Batteries. *Coord. Chem. Rev.* **2023**, *485*, 215142.

(21) Hoang Huy, V. P.; Hieu, L. T.; Hur, J. Zn Metal Anodes for Zn-Ion Batteries in Mild Aqueous Electrolytes: Challenges and Strategies. *Nanomaterials* **2021**, *11* (10), 2746.

(22) Peng, C.; Zhang, Y.; Yang, S.; Zhang, L. L.; Wang, Z. Flexible Zincophilic Polypyrrole Paper Interlayers for Stable Zn Metal Anodes: Higher Surface Flatness Promises Better Reversibility. *Nano Energy* **2022**, *98* (98), 107329.

(23) Zhang, Y.; Peng, C.; Zhang, Y.; Yang, S.; Zeng, Z.; Zhang, X.; Qie, L.; Zhang, L. L.; Wang, Z. In-Situ Crosslinked Zn2+-Conducting Polymer Complex Interphase with Synergistic Anion Shielding and Cation Regulation for High-Rate and Dendrite-Free Zinc Metal Anodes. *Chem. Eng. J.* **2022**, *448*, 137653.

(24) Cao, Q.; Gao, Y.; Pu, J.; Zhao, X.; Wang, Y.; Chen, J.; Guan, C. Gradient Design of Imprinted Anode for Stable Zn-Ion Batteries. *Nat. Commun.* **2023**, *14* (1), 641.

(25) Heiskanen, S. K.; Kim, J.; Lucht, B. L. Generation and Evolution of the Solid Electrolyte Interphase of Lithium-Ion Batteries. *Joule* **2019**, *3* (10), 2322−2333.

(26) Zheng, Z.; Zhong, X.; Zhang, Q.; Zhang, M.; Dai, L.; Xiao, X.; Xu, J.; Jiao, M.; Wang, B.; Li, H.; Jia, Y.; Mao, R.; Zhou, G. An Extended Substrate Screening Strategy Enabling a Low Lattice Mismatch for Highly Reversible Zinc Anodes. *Nat. Commun.* **2024**, *15* (1), 753.

(27) Huyan, X.; Yi, Z.; Sang, Z.; Tan, S.; Liu, J.; Chen, R.; Si, W.; Liang, J.; Hou, F. Polyethylene Glycol Coating on Zinc Powder Surface: Applications in Dendrite-Free Zinc Anodes with Enhanced Utilization Rate. *Appl. Surf. Sci.* **2023**, *614*, 156209.

(28) Xie, J.; Liang, Z.; Lu, Y. C. Molecular Crowding Electrolytes for High-Voltage Aqueous Batteries. *Nat. Mater.* **2020**, *19* (9), 1006−1011.

(29) Jin, L.; Jang, G.; Lim, H.; Zhang, W.; Park, S.; Jeon, M.; Jang, H.; Kim, W. Improving the Ionic Conductivity of PEGDMA-Based Polymer Electrolytes by Reducing the Interfacial Resistance for LIBs. *Polymers* **2022**, *14* (17), 3443.

(30) Hao, J.; Li, X.; Zhang, S.; Yang, F.; Zeng, X.; Zhang, S.; Bo, G.; Wang, C.; Guo, Z. Designing Dendrite-Free Zinc Anodes for Advanced Aqueous Zinc Batteries. *Adv. Funct. Mater.* **2020**, *30* (30), 1−10.

(31) Sakai, T. Gelation Mechanism and Mechanical Properties of Tetra-PEG Gel. *React. Funct. Polym.* **2013**, *73* (7), 898−903.

(32) Sugimura, A.; Asai, M.; Matsunaga, T.; Akagi, Y.; Sakai, T.; Noguchi, H.; Shibayama, M. Mechanical Properties of a Polymer Network of Tetra-PEG Gel. *Polym. J.* **2013**, *45* (3), 300−306.

(33) Wang, X. Y.; Wang, J. M.; Wang, Q. L.; Shao, H. B.; Zhang, J. Q. The Effects of Polyethylene Glycol (PEG) as an Electrolyte Additive on the Corrosion Behavior and Electrochemical Performances of Pure Aluminum in an Alkaline Zincate Solution. *Mater. Corros.* **2011**, *62* (12), 1149−1152.

(34) Mahalakshmi, S.; Hema, N.; Pp, V. In Vitro Biocompatibility and Antimicrobial Activities of Zinc Oxide Nanoparticles (ZnO NPs) Prepared by Chemical and Green Synthetic Route-A Comparative Study. *Bionanoscience* **2020**, *10* (1), 112−121.

(35) Max, J. J.; Chapados, C. Infrared Spectroscopy of Acetone−Water Liquid Mixtures. I. Factor Analysis. *J. Chem. Phys.* **2003**, *119* (11), 5632−5643.

(36) El Hadri, M.; Achahbar, A.; El Khamkhami, J.; Khelifa, B.; Faivre, V.; Cong, T. T.; Bougrioua, F.; Bresson, S. Raman Spectroscopy Investigation of Mono- and Diacyl-Polyoxyethylene Glycols. *Vib. Spectrosc.* **2013**, *64*, 78−88.

(37) Krishnan, K.; Krishnan, R. S. Raman and Infrared Spectra of Ethylene Glycol. *Proc. Natl. Acad. Sci., India, Sect. A* **1966**, *64*, 111−122.

(38) Subedi, D. P.; Madhup, D. K.; Sharma, A.; Joshi, U. M.; Huczko, A. Retracted: Study of the Wettability of ZnO Nanofilms. *Int. Nano Lett.* **2012**, *2* (1), 1−5.

(39) Pahari, D.; Das, N. S.; Das, B.; Chattopadhyay, K. K.; Banerjee, D. Tailoring the Optical and Hydrophobic Property of Zinc Oxide Nanorod by Coating with Amorphous Graphene. *Phys. E* **2016**, *83*, 47−55.

(40) Jia, H.; Wang, Z.; Dirican, M.; Qiu, S.; Chan, C. Y.; Fu, S.; Fei, B.; Zhang, X. A Liquid Metal Assisted Dendrite-Free Anode for High-Performance Zn-Ion Batteries. *J. Mater. Chem. A* **2021**, *9* (9), 5597−5605.

(41) Yu, J.; Peng, J.; Jia, X.; Wang, L.; Yang, K.; Zhao, J.; Yang, N. Modifying the Zn Anode with Nano-Silica: A Strategy to Realize Dendrite-Free Zinc-Ion Hybrid Supercapacitors. *J. Electrochem. Soc.* **2023**, *170* (2), 020508.

(42) Guazzelli, E.; Galli, G.; Martinelli, E. The Effect of Poly(Ethylene Glycol) (PEG) Length on the Wettability and Surface Chemistry of PEG-Fluoroalkyl-Modified Polystyrene Diblock Copolymers and Their Two-Layer Films with Elastomer Matrix. *Polymers* **2020**, *12* (6), 1236.

(43) Yang, C.; Tartaglino, U.; Persson, B. N. J. Influence of Surface Roughness on Superhydrophobicity. *Phys. Rev. Lett.* **2006**, *97* (11), 116103.

(44) Nguyen, T. L.; Blanquet, A.; Staiger, M. P.; Dias, G. J.; Woodfield, T. B. F. On the Role of Surface Roughness in the Corrosion of Pure Magnesium in Vitro. *J. Biomed. Mater. Res., Part B* **2012**, *100B* (5), 1310−1318.

(45) Cao, Z.; Zhu, X.; Gao, S.; Xu, D.; Wang, Z.; Ye, Z.; Wang, L.; Chen, B.; Li, L.; Ye, M.; Shen, J. Ultrastable Zinc Anode by Simultaneously Manipulating Solvation Sheath and Inducing Oriented Deposition with PEG Stability Promoter. *Small* **2022**, *18* (6), 1−8.

(46) Pei, A.; Zheng, G.; Shi, F.; Li, Y.; Cui, Y. Nanoscale Nucleation and Growth of Electrodeposited Lithium Metal. *Nano Lett.* **2017**, *17*, 1132−1139.

(47) Liu, Z.; Liu, J.; Xiao, X.; Zheng, Z.; Zhong, X.; Fu, Q.; Wang, S.; Zhou, G. Unraveling Paradoxical Effects of Large Current Density on Zn Deposition. *Adv. Mater.* **2024**, *36*, 2404140.

(48) Kim, M.; Lee, J.; Kim, Y.; Park, Y.; Kim, H.; Choi, J. W. Surface Overpotential as a Key Metric for the Discharge-Charge Reversibility of Aqueous Zinc-Ion Batteries. *J. Am. Chem. Soc.* **2023**, *145* (29), 15776−15787.

(49) Ilic, S.; Counihan, M. J.; Lavan, S. N.; Yang, Y.; Jiang, Y.; Dhakal, D.; Mars, J.; Antonio, E. N.; Kitsu Iglesias, L.; Fister, T. T.; Zhang, Y.; Maginn, E. J.; Toney, M. F.; Klie, R. F.; Connell, J. G.; Tepavcevic, S. Effect of Antisolvent Additives in Aqueous Zinc Sulfate Electrolytes for Zinc Metal Anodes: The Case of Acetonitrile. *ACS Energy Lett.* **2024**, *9* (1), 201−208.

(50) Cao, Q.; Pan, Z.; Gao, Y.; Pu, J.; Fu, G.; Cheng, G.; Guan, C. Stable Imprinted Zincophilic Zn Anodes with High Capacity. *Adv. Funct. Mater.* **2022**, *32*, 2205771.

(51) Wang, Y.; Deng, Y.; Liu, J.; Zhang, B.; Chen, Q.; Cheng, C. Three-Dimensional Ordered Macroporous Flexible Electrode Design toward High-Performance Zinc-Ion Batteries. *ACS Appl. Mater. Interfaces* **2024**, *16* (10), 12697−12705.

(52) He, H.; Zeng, L.; Luo, D.; He, J.; Li, X.; Guo, Z.; Zhang, C. 3D Printing of Electron/Ion-Flux Dual-Gradient Anodes for Dendrite-Free Zinc Batteries. *Adv. Mater.* **2023**, *35* (17), 2211498.

(53) Zhang, Q.; Luan, J.; Huang, X.; Zhu, L.; Tang, Y.; Ji, X.; Wang, H. Simultaneously Regulating the Ion Distribution and Electric Field to Achieve Dendrite-Free Zn Anode. *Small* **2020**, *16* (35), 2000929.

(54) Stephen, A.; Engineering, M.; Texas, N. 3D - Printed Flexible Anode for High - Performance Zinc Ion Battery. *MRS Commun.* **2022**, *12* (5), 894−901.

(55) Xie, S.; Li, Y.; Li, X.; Zhou, Y.; Dang, Z.; Rong, J.; Dong, L. Stable Zinc Anodes Enabled by Zincophilic Cu Nanowire Networks. *Nano-Micro Lett.* **2022**, *14* (1), 39.

(56) Zhang, G.; Zhang, X.; Liu, H.; Li, J.; Chen, Y.; Duan, H. 3D-Printed Multi-Channel Metal Lattices Enabling Localized Electric-Field Redistribution for Dendrite-Free Aqueous Zn Ion Batteries. *Adv. Energy Mater.* **2021**, *11*, 2003927.